Imaging Lithium Atoms at Sub-Ångstrom Resolution

Michael A. O'Keefe* and Yang Shao-Horn**

*Materials Sciences Division, Lawrence Berkeley National Laboratory,
1 Cyclotron Road, Berkeley, CA 94720, U.S.A.

**Department of Mechanical Engineering, Massachusetts Institute of Technology,
77 Massachusetts Avenue, Cambridge, MA 02139, U.S.A.

This article originally appeared in a shortened form in Microscopy and Microanalysis **10** (2004) 86-95, and it is reprinted here by special arrangement with Cambridge University Press and the Microscopy Society of America.

Corresponding Author: Michael A. O'Keefe,
email maok@lbl.gov
phone 510-486-4610
fax: 510-486-5530
mailing address: LBNL MS 2R200, 1 Cyclotron Road, Berkeley, CA 94720, USA

Running head: Sub-Ångstrom Imaging of Light Atoms

DISCLAIMER

This document was prepared as an account of work sponsored by the United States Government. While this document is believed to contain correct information, neither the United States Government nor any agency thereof, nor The Regents of the University of California, nor any of their employees, makes any warranty, express or implied, or assumes any legal responsibility for the accuracy, completeness, or usefulness of any information, apparatus, product, or process disclosed, or represents that its use would not infringe privately owned rights. Reference herein to any specific commercial product, process, or service by its trade name, trademark, manufacturer, or otherwise, does not necessarily constitute or imply its endorsement, recommendation, or favoring by the United States Government or any agency thereof, or The Regents of the University of California. The views and opinions of authors expressed herein do not necessarily state or reflect those of the United States Government or any agency thereof, or The Regents of the University of California.

Ernest Orlando Lawrence Berkeley National Laboratory is an equal opportunity employer.

Lawrence Berkeley National Laboratory -- LBNL-56646

Imaging Lithium Atoms at Sub-Ångstrom Resolution

Michael A. O'Keefe* and Yang Shao-Horn**

*Materials Sciences Division, Lawrence Berkeley National Laboratory, 1 Cyclotron Road,
Berkeley, CA 94720

**Department of Mechanical Engineering, Massachusetts Institute of Technology,
77 Massachusetts Avenue, Cambridge, MA 02139

ABSTRACT

John Cowley and his group at ASU were pioneers in the use of transmission electron microscopy (TEM) for high-resolution imaging. Three decades ago they achieved images showing the crystal unit cell content at better than 4Å resolution. Over the years, this achievement has inspired improvements in resolution that have enabled researchers to pinpoint the positions of heavy atom columns within the cell. More recently, this ability has been extended to light atoms as resolution has improved. Sub-Ångstrom resolution has enabled researchers to image the columns of light atoms (carbon, oxygen and nitrogen) that are present in many complex structures. By using sub-Ångstrom focal-series reconstruction of the specimen exit surface wave to image columns of cobalt, oxygen, and lithium atoms in a transition metal oxide structure commonly used as positive electrodes in lithium rechargeable batteries, we show that the range of detectable light atoms extends to lithium. HRTEM at sub-Ångstrom resolution will provide the essential role of experimental verification for the emergent nanotech revolution. Our results foreshadow those to be expected from next-generation TEMs with C_S-corrected lenses and monochromated electron beams.

KEYWORDS: sub-Ångstrom, atomic-resolution, HREM, lithium battery, FSR, ESW, TrueImage

INTRODUCTION

Resolution was first defined in terms of the classic case of separation of adjacent objects (Rayleigh, 1874). Considerations of noise and coherence in detected images require modification of this simple definition (for a thorough discussion see den Dekker & van den Bos, 1997). Nevertheless, resolution requires the ability to produce images showing distinct separation of discrete objects (in the case of high-resolution TEM, discrete peaks corresponding to atoms, or to columns of atoms seen end-on). Note that demonstration of a resolution of $|\mathbf{d}|$ requires the presence of the corresponding spatial frequency $1/|\mathbf{d}|$ in the image diffractogram (either the intensity spectrum or the power spectrum). However, the mere presence of the $1/|\mathbf{d}|$ frequency is not sufficient to establish a corresponding resolution of $|\mathbf{d}|$ (O'Keefe, 1979).

Resolution can be thought of in terms of the number of significant (non-empty) sampling points in the image – the finer the real-space sampling of the electron wave (at the specimen exit surface) that the microscope can image, the higher is its resolution. Higher resolution not only allows the separation of closer objects, the finer sampling improves the detection of weaker signals, thus making possible the imaging of lighter atoms in the presence of heavier ones.

Improvements in resolution can result in more accurate measurement of physical properties. In turn, the improved measurements made possible by higher resolution can lead to new understandings of the reasons for these properties. Over the past three decades, improvements in transmission electron microscope (TEM) resolution have enabled materials scientists to move from general observations of large-scale defects (grain boundaries, dislocations) to studies of details within the crystal unit cell. Recent advances have allowed the imaging of all the atoms within the unit cell, as well as the study of non-periodic defects at the atomic level.

BACKGROUND

Early studies at 7Å resolution revealed the positions of crystallographic shear planes within unit cells of transition metal oxides (Allpress, 1969). Positions of metal-oxide octahedra appeared at 3.5Å resolution (Iijima, 1971). Individual metal-atom columns became accessible in alloys at 1.8-2.0Å resolution (Cook et al., 1983), and in silicates at 1.6Å resolution (Epicier et al., 1990). Software for simulation of HREM images from structural models was able to explain the images and confirm interpretations of them, (Allpress et al., 1972; Lynch & O'Keefe, 1972; Anstis et al., 1973; O'Keefe, 1973; Lynch at al, 1975; O'Keefe & Sanders, 1975: O'Keefe et al., 1978).

Resolution limits, set by phase changes imposed by spherical aberration (Scherzer, 1949), remain close to 1.5Å for uncorrected mid-voltage TEMs and 1Å for high-voltage (≥1MV) TEMs. Methods to overcome the "Scherzer limit" by correcting for phase changes include focal-series reconstruction of the electron wave at the specimen exit surface (Schiske, 1973; Van Dyck & Op de Beeck 1990), holography (Lichte, 1991), and hardware correction of C_S (Haider et al., 1995).

A simple linear reconstruction, from five to ten images obtained over a range of focus values, improved the resolution of an image of staurolite obtained on a JEOL ARM-1000 from 1.6Å to 1.38Å and allowed the imaging of oxygen atoms (Wenk et al., 1992). Following on from this result, the One-Ångstrom Microscope (OÅM) project (O'Keefe, 1993; O'Keefe et al., 2001b) was created to attain sub-Ångstrom resolution using FEI's TrueImage software for focal-series reconstruction (Coene et al., 1996; Thust et al., 1996) from images obtained on a CM300FEG/UT modified to improve its information limit. The CM300FEG/UT-OÅM has been shown to be capable of successfully generating the specimen exit-surface wave (ESW) to 0.89Å resolution in diamond (Wang et al., 1999), and to 0.78Å in silicon (O'Keefe et al., 2001a; O'Keefe, 2004).

THEORY

Image Formation

In the HRTEM, the image is recorded with an intensity, $I(\mathbf{x})$, which is the square of the complex image amplitude, or electron wave, $\psi(\mathbf{x})$ at the image plane:

$$I(\mathbf{x}) \; = \; \psi(\mathbf{x})\,\psi^*(\mathbf{x}) \tag{1}$$

Fourier transformation of this equation gives the image intensity spectrum as the auto-correlation function of the image amplitude spectrum, $\Psi(\mathbf{u})$

$$I(\mathbf{u}) = \Psi^*(-\mathbf{u}) \otimes \Psi(\mathbf{u}) \tag{2}$$

where $\otimes$ represents convolution.

The convolution may be written out as a sum over all pairs of amplitude spectrum components, $\Psi(\mathbf{u})$ that contribute to the image, in the form

$$I(\mathbf{u}) = \sum_{\mathbf{u}'} \Psi(\mathbf{u}') \,.\, \Psi^*(\mathbf{u}'\text{-}\mathbf{u}) \tag{3}$$

where each product term represents the contribution to the image intensity spectrum of the interference of any complex diffracted beam amplitude $\Psi(\mathbf{u}')$ with (the conjugate of) all the complex diffracted beam amplitudes $\Psi^*(\mathbf{u}'\text{-}\mathbf{u})$.

Phase changes from the objective lens are imposed on the specimen exit-surface wave $\Psi_E(\mathbf{u})$, to produce the image amplitude spectrum wave $\Psi(\mathbf{u})$. The phase changes are described via an objective lens phase function $\chi(\mathbf{u})$, such that

$$\Psi(\mathbf{u}) = \Psi_{\mathbf{E}}(\mathbf{u}).\exp\{-i\chi(\mathbf{u})\} \qquad (4)$$

Then the image intensity spectrum is given by

$$I(\mathbf{u}) = \sum_{\mathbf{u'}} \Psi_{\mathbf{E}}(\mathbf{u'}).\exp\{-i\chi(\mathbf{u'})\}\,.\,\Psi_{\mathbf{E}}^{*}(\mathbf{u'-u}).\exp\{+i\chi(\mathbf{u'-u})\} \qquad (5)$$

For a specimen that scatters weakly, such as a thin specimen or a thicker one that is not precisely oriented down a zone-axis, the major contributions to the image intensity spectrum will come from terms that contain the interference of a diffracted beam with the central (000) beam. Beam-beam interference that does not include the 000 beam (the so-called "second order" or "non-linear" interference) will contribute only weakly for such a specimen (O'Keefe, 1979). Under this condition, we can neglect non-linear interference and consider just linear interference with the 000 beam. It can then be shown that only one pair of diffracted beams contributes to each spatial frequency in the image intensity spectrum, and that this pair comes from *one* coefficient of the projected specimen potential (O'Keefe, 1992).

With non-linear terms excluded from eqn.5, the **u**th component of the "linear-image" intensity spectrum contains only **u** and **-u** diffracted-beam interference with the zero beam

$$I_L(\mathbf{u}) = \Psi_{\mathbf{E}}(\mathbf{u}) \exp\{-i\chi(\mathbf{u})\}\,.\,\Psi_{\mathbf{E}}^{*}(\mathbf{0}) + \Psi_{\mathbf{E}}(\mathbf{0}).\Psi_{\mathbf{E}}^{*}(\mathbf{-u}) \exp\{+i\chi(\mathbf{-u})\} \qquad (6)$$

$\Psi(\mathbf{0})$ has a weight that is close to unity for a weakly-scattering specimen. Since it is present for all the interference terms and can be normalized out, we can write

$$I_L(\mathbf{u}) = \Psi_{\mathbf{E}}(\mathbf{u}).\exp[-i\chi(\mathbf{u})] + \Psi_{\mathbf{E}}^{*}(\mathbf{-u}).\exp[+i\chi(\mathbf{-u})] \qquad (7)$$

The electron wave at the specimen exit surface is a function of the (projected) specimen structure. The major effect of elastic scattering of the electrons within the specimen occurs on the phase of the electron wave traversing the specimen – the specimen behaves as a "phase object". Thus, information about the (projected) spatial distribution of specimen potential $\phi_p(\mathbf{x})$ and specimen thickness H is encoded in the phase of the electron wave, which can be written

$$\psi_E(\mathbf{x}) = \exp\{-i\,\sigma\,\phi_p(\mathbf{x})\,H\} \qquad (8)$$

where σ is an interaction parameter that is weakly dependent on electron energy.

For our weakly-scattering specimen, the majority of the elastically-scattered electrons will undergo kinematic (single) scattering. Neglecting dynamical diffraction, the direct-space electron wave at the specimen exit-surface of this "weak phase object" can then be written

$$\psi_E(\mathbf{x}) = 1 - i\,\sigma\,\phi_p(\mathbf{x})\,H \qquad (9)$$

where σ is the interaction coefficient, $\phi_p(\mathbf{x})$ is the specimen potential projected in the incident electron beam direction, and H is the specimen thickness. In Fourier space

$$\Psi_E(\mathbf{u}) = \delta(\mathbf{u}) - i\,\sigma\,V(\mathbf{u})\,H \qquad (10)$$

where $V(\mathbf{u})$ is the (complex) Fourier component, with spatial frequency $\mathbf{u}$, of the (real) projected potential $\phi_p(\mathbf{x})$.

When the (reciprocal-space) exit-surface wave (10) is included, the expression for the linear image intensity spectrum (7) becomes

$$I_L(\mathbf{u}) = \delta(\mathbf{u}) - i\,\sigma\,V(\mathbf{u})\,H\exp[i\chi(\mathbf{u})] + i\,\sigma\,V^*(-\mathbf{u})\,H\exp[-i\chi(-\mathbf{u})] \qquad (11)$$

Then, since $\{\exp[i\chi(\mathbf{u})] - \exp[-i\chi(-\mathbf{u})]\}$ is equal to $2i\sin\chi(\mathbf{u})$ for a round lens, and $V^*(-\mathbf{u})$ is equal to $V(\mathbf{u})$ for a real potential, the image intensity spectrum for such a "linear" (or "weak-phase object") image is reduced to

$$I_L(\mathbf{u}) = \delta(\mathbf{u}) + 2\sigma V(\mathbf{u}) H \sin\chi(\mathbf{u}) \qquad (12)$$

Thus the magnitude of the **u**th term in the image intensity spectrum is just proportional to $V(\mathbf{u})$, which is the **u**th Fourier coefficient of the projected potential, and to $\sin\chi(\mathbf{u})$, the value of the phase-contrast transfer function (CTF) at the corresponding value of $|\mathbf{u}|$.

By choosing a value of defocus at which $\sin\chi(\mathbf{u})$ is approximately equal to –1 (Scherzer or optimum defocus), it is possible to have each term in the intensity spectrum proportional to (the negative of) the corresponding Fourier coefficient of the projected potential. An inverse Fourier transformation back into direct space yields image intensity proportional to the negative magnitude of the projected potential. Peaks in the potential at the atom positions will produce dips in the image intensity; the image will show "black atoms".

$$I_L(\mathbf{x}) = 1 - 2\sigma\phi_p(\mathbf{x}) H \qquad (13)$$

Phase

Electron microscope imaging theory requires several complex functions, so several phases are involved. One is the phase of the real-space electron wave exiting the specimen (the ESW), and others are the phases of reciprocal-space components of real-space functions. It is important that clear distinctions be maintained about the roles of these phases in the description of electron scattering and their effects on the microscope image.

Structure Factor Phase: The incoming electron wave "sees" the specimen potential $\phi_p(\mathbf{x})$ and is modulated by it. The image is ultimately a function of this potential (projected in the beam direction and filtered by the objective lens). The specimen potential $\phi_p(\mathbf{x})$ is described in Fourier space by a set of structure factors V($\mathbf{u}$). Although the potential is real, the structure factors are complex and possess magnitudes and phases. The magnitudes of the structure factors give the relative weights of the spacings contained in the potential distribution, and the phases give their positions (a phase change in reciprocal space is a shift in real space). In structure determination, the difficulty of measurement of these phases is known as "the phase problem".

Electron Wave Phase: The real-space electron wave exiting the specimen (the ESW) carries information about the specimen in the form of a spatial distribution of phase changes. The relative phase of the wave is $\sigma\phi_p(\mathbf{x})\,H$, where σ is the interaction parameter, H is specimen thickness, and $\phi_p(\mathbf{x})$ is the (projected) spatial distribution of specimen potential per unit thickness (eqn.8). This phase depends linearly on specimen thickness (the number of atoms stacked in the beam direction), and its spatial distribution shows the positions of the atom columns and the relative scattering power of the type of atom in each column.

Objective Lens Phase: The electron wave exiting the specimen (the ESW) passes through the objective lens. Diffracted beams (Fourier component of the ESW) suffer phase changes as they are brought together by the lens to interfere and form the image intensity spectrum. These phase changes depend on many lens parameters and aberrations, the chief of which are defocus and spherical aberration. Phase changes introduced by the objective lens on the components of the electron wave (the diffracted beams) are described by the lens phase function $\chi(\mathbf{u})$.

Image Intensity-Spectrum Phase: The electron wave is recorded as an image, and the Fourier transform of the image is the image intensity spectrum (eqn.5). The magnitudes of the components of the image intensity spectrum can be seen in the diffractogram of the image. The relative phases of the components determine the relative positions of the spacings in the image and thus its accuracy in representing the specimen structure.

Phase Interactions and Scherzer Imaging: The electron wave exiting the specimen (the ESW) is modified by the phase changes described by the objective lens transfer function (the PTF). The transfer of ESW phase into image intensity is governed by the contrast transfer function (CTF) as a function of spatial frequency (eqn.12). It is possible to adjust the lens so that the PTF adds approximately the same phase change to the ESW at all spatial frequencies out to the resolution limit of the microscope (and also that the CTF transfer is maximized and approximately constant to the same limit). Under these conditions (Scherzer, 1949) the relative phase of each component (at each spatial frequency) of the image-plane wave is the same as that at the corresponding spatial frequency in the ESW. Additionally, with the spatial distribution of the ESW phase properly mapped into the phase of the image-plane wave, there will be no "phase problem" for the structure factors, and the image will display the projected potential of the specimen to the resolution limit of the microscope (eqn.13).

The image will be accurate only when all the phases work together. For a properly oriented thin specimen, structure factor phases will be correctly transferred into the ESW phase; correctly chosen lens phase changes will preserve the relative phase of the ESW in the image. The image will then possess the same relative phases in the terms of its intensity spectrum as the relative phases of the structure factors. However, if the lens imposes a phase change that varies significantly with spatial frequency, the spatial distribution of the ESW phase will be mapped into the image with phase distortions, and the image will not show the positions and relative weights of atom columns accurately.

Phase Interactions and Focal Series Reconstruction: The electron wave exiting the specimen (the ESW) can be reconstructed numerically to an extent that depends on the accuracy with which we can measure the recorded image intensity and characterize the (complex) PTF of the lens. By measuring the lens parameters and recording a series of images at known values of defocus, it is possible to apply a parabolic reconstruction method (Van Dyck & Op de Beeck, 1990) to generate a first estimate of the ESW to the resolution of the highest spatial frequency recorded in the images. This first estimate can then be improved by using a method of maximum likelihood to refine the estimates of the experimental parameters (Coene et al., 1996; Thust et al., 1996). The FEI TrueImage software combines both methods. In effect, the focal series reconstruction technique removes the phase effects of the microscope lens and produces the complex ESW from the recorded image intensities and the known lens phase changes that produced them. For a specimen that scatters sufficiently weakly to be treated as a phase object, the spatial distribution of the relative phase of the complex ESW should map the specimen (projected) potential (eqn.8). The relative phase of the ESW should depend linearly on specimen thickness (the number of atoms stacked up in the beam direction), and its spatial distribution should reveal the positions of the atom columns and the relative scattering power of the type of atom contributing to each column. In addition, once the complex ESW has been determined, it is possible to produce any desired image of the experimental specimen by adding an appropriate "lens function" in the computer (Thust, 200x).

Focal-series reconstruction is used to remove microscope lens effects and to find the ESW (and in particular its phase) to a resolution limited only by the microscope information limit. Since the (real space) phase of the ESW is an entirely different function from the (reciprocal space) phases of the specimen structure factors, removal of the phase factors of the microscope lens to obtain the phase of the ESW does not constitute a direct solution to the "phase problem". In fact, information about relative atom column positions and weights is present in the same form in both the reconstructed ESW (where it occurs as $\sigma\,\phi_p(\mathbf{x})\,H$ in the relative phase of the ESW) and in the Scherzer image (where it takes the form $1 - 2\,\sigma\,\phi_p(\mathbf{x})\,H$ in the image intensity). Thus Scherzer imaging and ESW phase both provide the same information about the phase of the structure factors, and hence the positions and weights of atom columns (O'Keefe, 2004).

Of course, in order to contain the same information about the atoms that make up the specimen, both the ESW phase and the Scherzer image must contain Fourier components out to the same spatial frequency, i.e., they must have the same resolution. The advantage of focal-series reconstruction is that it can be used to form the ESW to a much higher spatial frequency (better resolution) than the Scherzer image (at least any obtained from a HRTEM without an objective lens aberration corrector). In effect, focal-series reconstruction acts as a software aberration corrector and allows the use of spatial frequencies out to the microscope information limit, thus improving the microscope resolution to this limit (O'Keefe et al, 2001b). As well as resolution improvement, another advantage of focal-series reconstruction over Scherzer imaging is that the specimen can be thicker, since it need only satisfy "phase object" conditions (eqn.8) instead of the "weak phase object" condition (eqn.9) required by Scherzer imaging. In addition, reduced second-order "non-linear" components in the reconstructed phase image allow for a thicker specimen and a cleaner result compared with a Scherzer image.

Resolution

Scherzer's (1949) optimum defocus condition maximizes the range of spatial frequencies for which the objective lens phase transfer function $\chi(\mathbf{u})$ (eqn.14) is approximately constant and close to $-\pi/2$ ($\sin\chi = -1$). Then the resolution of the electron microscope corresponds to the highest spatial frequency that is transferred into the image intensity spectrum with the same sign as all lower contributing frequencies. Beyond the "Scherzer cut-off frequency", $\sin\chi(\mathbf{u})$ changes sign, and higher-frequency Fourier components of the potential can contribute to the linear image with opposite sign. An image containing a mixture of spatial frequencies transferred with mixed signs is, in general, no longer interpretable intuitively and generally requires comparison with image simulations for interpretation (O'Keefe et al, 1978).

The phase change due to objective lens defocus ε and spherical aberration coefficient C_S at an electron wavelength λ is

$$\chi(\mathbf{u}) = \pi\varepsilon\lambda|\mathbf{u}|^2 + \pi C_S\lambda^3|\mathbf{u}|^4/2 \qquad (14)$$

When ?($\mathbf{u}$) is set equal to zero in equation (14), the cutoff (zero-crossing) frequency is given by

$$|\mathbf{u}| = \sqrt{\{-2\varepsilon/(C_S\lambda^2)\}} \qquad (15)$$

Setting defocus at the Scherzer value of $\varepsilon = -\sqrt{(C_S\lambda)}$ gives a cutoff at $|\mathbf{u}| = \sqrt{2}C_S^{-1/4}\lambda^{-3/4}$ (or $1.414C_S^{-1/4}\lambda^{-3/4}$). Careful comparisons of simulated WPO with simulated high-resolution lattice image (SHRLI) images showed that the cutoff frequency could be extended to $6^{1/4}C_S^{-1/4}\lambda^{-3/4}$ (or $1.565C_S^{-1/4}\lambda^{-3/4}$) by choosing a defocus of $\varepsilon = -\sqrt{(3C_S\lambda/2)}$ giving the Scherzer resolution of the microscope as

$$d_S = 0.64\, C_S^{1/4}\, \lambda^{3/4} \qquad (16)$$

Information Limit

The incident electron beam has partial spatial and temporal coherence. Like the Scherzer phase limit, these factors impose limits on how high a spatial frequency can be transferred from the exit-surface wave to the image. Partial temporal coherence manifests as spread of focus, and partial spatial coherence as incident beam convergence (O'Keefe and Sanders, 1975). These effects restrict transfer and attenuate the microscope CTF with 'damping envelope' functions (Frank 1973, Wade and Frank 1977).

The CTF damping envelope function for temporal incoherence has the form

$$E_\Delta(\mathbf{u}) = \exp\{-\tfrac{1}{2}\pi^2\lambda^2\Delta^2|\mathbf{u}|^4\} \qquad (17)$$

where Δ is the standard deviation of a Gaussian spread-of-focus. The damping envelope reduces transfer to a level of exp(-2) or 13.5% at the cutoff frequency $|\mathbf{u}|_\Delta = (\pi\lambda\Delta/2)^{-1/2}$, leading to an absolute information limit for the microscope of

$$d_\Delta = 1/|\mathbf{u}|_\Delta = \sqrt{(\pi\lambda\Delta/2)} \qquad (18)$$

The Δ parameter includes effects that change microscope focus over the image acquisition time, such as lens current ripple and high-voltage noise and ripple, as well as incident beam energy spread due to intrinsic gun spread and the Boersch contribution (O'Keefe et al., 2002). Then

$$\Delta = C_C\sqrt{\{4\sigma^2(I)/I^2 + \sigma^2(E)/E^2\}} \qquad (19)$$

where C_C is the chromatic aberration coefficient for the objective lens, σ(I)/I is the fractional rms ripple in lens current, and σ(E)/E is the rms energy spread in the electron beam (including high-voltage noise and ripple) as a fraction of the total beam energy.

Spatial Coherence

The damping envelope function for a Gaussian-weighted incident beam convergence is

$$E_\alpha(\mathbf{u}) = \exp\{-\pi^2\alpha^2(\varepsilon+\lambda^2 C_S\mathbf{u}^2)^2\mathbf{u}^2\} \qquad (20)$$

where α is the standard deviation of a Gaussian over the range of angles in the convergent cone; α is 0.77 times the measured semi-angle (Malm and O'Keefe, 1993).

Convergence and spread of focus impose limits on lens transfer at higher spatial frequencies. The convergence limit varies with defocus and does not impose an absolute limit to microscope information transfer, unlike the spread of focus.

METHODS

Initial Observations

Early HRTEM images of metal oxides, such as $Ti_2Nb_{10}O_{29}$, taken at Scherzer defocus (Iijima, 1971), showed projections of the structure at spacings down to the 3.8Å tunnels between metal-oxygen octahedra (Fig. 1a). Images of the same areas obtained at larger values of underfocus contained confusing mixtures of spacings, but sometimes showed finer details of the structure than images at Scherzer defocus (Fig. 1b). In the case of $Ti_2Nb_{10}O_{29}$, the image at twice the Scherzer underfocus is no longer a projection showing the 3.8Å tunnels within blocks of metal-oxygen octahedra, but simulations confirmed that it shows the 2.8Å tunnels between overlapping blocks (Fig. 1b), with the 3.8Å tunnels missing (Anstis & O'Keefe, 1976).

Because the mid and high frequencies (large and small tunnels) are spatially separated, $Ti_2Nb_{10}O_{29}$ is a good example to illustrate how transfer changes with defocus. However, in many structures these different spacings overlap. In such structures, defocus to non-Scherzer values will appear to produce shifted or missing "atoms" (i.e., spots that can be misinterpreted as atom positions), or even to add spurious "atoms" to the image.

Because increased underfocus provides smaller details, it is possible to test model structures by comparing an experimental focal series with a simulated focal series (e.g., Epicier et al., 1990). However, the fit of experiment and simulation is distributed over several images and it is difficult to get an idea of the "goodness" of the match. A more-convenient way to compare a model and experimental images would obviously be to combine information from several images – in effect, using the post-resolution information to extend the microscope resolution to its information limit – to produce one image containing properly-phased spacings at both mid and high frequencies. In the course of a 3-D reconstruction experiment (Downing et al., 1990), the resolution of a JEOL ARM-1000 was improved from a normal 1.6Å to 1.38Å by combining information from focal series of five to ten images of a staurolite specimen (Wenk et al., 1992). The result was confirmed by image simulation (Fig. 2).

One consequence of improved resolution is the ability to image lighter atoms. Focal series reconstruction from five staurolite images clearly shows oxygen atoms at 1.38Å resolution in the reconstructed image (Fig. 2c), particularly the oxygen-metal-oxygen string positioned vertically in the center of the unit cell (Wenk et al., 1992). Oxygen atoms also appear at similar resolutions (1.4-1.5Å) in images of ZrO_2 obtained at 1.3MeV (Horiuchi et al., 1991), in focal-series reconstructions of $BaTiO_3$ (Jia & Thust, 1999), and in C_S-corrected images of perovskites (Jia et al., 2003). Reconstruction at sub-Ångstrom resolution has produced images showing even lighter atoms, including carbon (O'Keefe at al, 2001b) and nitrogen (Kisielowski et al., 2001).

Sub-Ångstrom Microscopy

For the best-possible resolution, a microscope should have a very good information limit and a means to extend its resolution to that limit. Information limit is a function of the microscope's spread of focus (eqn. 18) and is strongly dependent on the total energy spread in the incident electron beam (eqn. 19). To keep energy spread low, we require a microscope with a field-emission electron source. Such a microscope can be used to produce sub-Ångstrom resolution by phase correction (either with holography or by focal-series reconstruction). The One-Ångstrom Microscope (OÅM-CM300FEG/UT) is a combination of reconstruction software with a highly stable field-emission TEM (O'Keefe, 1993).

The hardware part of the OÅM is an improved CM300FEG/UT. Originally, the CM300FEG/UT had lens current and high-voltage power supplies stable to one part per million for a spread of focus of 36Å and an information limit of 1.07Å (Bakker et al., 1996). The CM300FEG/UT-OÅM uses improved power supplies with better stabilities to achieve beam energy spread of 0.85eV FWHH (O'Keefe et al., 2002), spread of focus of 20Å, and information limit of 0.78Å (O'Keefe et al., 2001b). CTFs reveal that, although the Scherzer resolution (the upper limit of the main passband) remains the same for the two microscopes, the smaller spread of focus of the OÅM-CM300FEG/UT extends the information limit from the 1.07Å of the standard CM300 (Fig. 3a) to 0.78Å (Fig. 3b).

The software part of the OÅM uses the FEI TrueImage focal-series reconstruction code (Coene et al., 1996; Thust et al., 1996) to compute an estimate of the sample exit-surface electron wave

(ESW) from a focal series of ten to twenty images. Resolution in the computed ESW is limited only by the highest spatial frequency contained in the images of the focal series. Under proper conditions, the series can contain information to the information limit of the microscope (O'Keefe, 2001). The final result is the phase of the ESW, since the phase should be proportional to a projection of the specimen structure (Cowley & Iijima, 1972).

Spatial Coherence

Although it does not contribute to the information limit, spatial coherence can limit transfer into any given image. At Scherzer defocus, the OÅM's temporal-coherence-limited CTF (Fig. 3b) is severely damped at higher frequencies when the incident beam convergence of $\alpha = 0.25$ milli-radian is applied (Fig. 3c). Increasing the microscope underfocus improves transfer at higher spatial frequencies, only slightly for the second-passband ($n = 2$) condition (Fig. 3d), but more for higher-passband conditions (Fig. 3e). For $n = 36$, the main transfer extends from 0.93Å to 0.85Å. However, at high underfocus there is reduced transfer of midrange frequencies.

The effects of defocus exhibited by images of $Ti_2Nb_{10}O_{29}$ (Fig. 1), may be illustrated by the CTFs of figure 3 (even though these are computed for different resolution). The main passband moves to higher frequencies in going from the $n=0$ condition (Fig. 3c) to the $n=2$ condition (Fig. 3d). For the JEOL 100B the defocus change moved the main passband from a spatial frequency that imaged the large tunnels (Fig. 1a) to a higher spatial frequency able to image the small tunnels (Fig. 1b). Of course, the same defocus change also misphased the spatial frequency of the large tunnels by introducing a positive-going mid-range peak (Fig. 3d), resulting in scrambled contrast at the large tunnel positions.

Another way to examine effects of spatial coherence on transfer into the image is to plot a focus-variation transfer function (FVTF). Just as a CTF shows transfer at one defocus over a range of spatial frequencies, a FVTF shows transfer at one frequency over a range of defocus (O'Keefe at al, 2001a,b). The FVTF separates the effects of spherical aberration from convergence, and shows how transfer of any particular spatial frequency u_{hkl} is confined to a Gaussian packet with a defocus range centered on the alpha-null defocus of ε_α^o $(u_{hkl}) = - C_S (\lambda\ u_{hkl})^2$. The packet width is independent of C_S and is a function of the convergence semiangle α. At a cutoff value where packet transfer drops to exp(-2), the packet width is $\pm\,\varepsilon_\alpha^{2\sigma}(u_{hkl}) = \pm\sqrt{2}/\{\pi\,\alpha\,u_{hkl}\}$.

To image carbon atoms at the correct positions in a [110] "dumbbell" image from a test specimen of diamond, the final image must include contributions from all four sets of diffracted beams out to the 004 spacing of 0.89Å. The FVTF for [110] diamond (Fig. 4) shows how transfer at the four diffracted-beam frequencies is confined to four defocus packets centered on the alpha-null defocus of each spatial frequency. Within the packets, the diffracted beam phases (and thus the transfer strengths) oscillate at periods that are integer sub-multiples of the Fourier image period for the projected unit cell. For a unit cell parameter of **d**, the diffracted beams reach identical relative phases (and produce identical images) at defocus periods of $2|\mathbf{d}|^2/\lambda$. Proposed for light optics by Cowley & Moodie (1957a), the Fourier image effect was first demonstrated for electrons by Iijima and O'Keefe (1979). Subsequently, it has been shown that the Fourier image defocus range is confined to the region of overlap of the FVTF packets for extended-resolution conditions (O'Keefe et al., 2001b).

For a convergence semiangle as large as 0.25 milliradian, the packets are still sufficiently broad to allow substantial overlap in defocus. In the case of diamond, the overlap under OÅM conditions extends from the lower limit of the 004 packet to the upper limit of the 113 (and 022) packets (Fig. 4). Within this overlap range, it is possible to obtain a full range of Fourier images with contributions from all the beams and a resolution corresponding to the 004 spacing (0.89Å). To form a reliable high-resolution image requires that transfer from all the diffracted beams be approximately equal. Since each packet is attenuated by spread of focus damping (the 004 packet has a maximum excursion only 28% of that of the 111 packet), optimum defocus is close to that at which all the packets have about the same height, at approximately -3000Å (Fig. 4).

Three-fold Astigmatism

One requirement for sub-Ångstrom imaging is correction of the objective lens three-fold astigmatism. Prior to correction, a test specimen of [110] diamond, imaged under overlap conditions (Fig. 4), produced a non-intuitive image. The image failed to show the expected "dumbbell" character (Fig. 5a), although a Fourier transform showed the [110] pattern with a very weak 004 spot (Fig. 5b). Averaging of the experimental image produced a three-fold pattern (Fig. 5c) that could be matched by a simulated image (Fig. 5d) only when a three-fold astigmatism value of 2.25µm was included (O'Keefe, 1998). Interestingly, changing the phases of the spots making up the image intensity spectrum by imposition of the known diamond symmetry, first as a vertical mirror (Fig. 5e), then as a horizontal one (Fig. 5f), produced an image that was close to the expected symmetry. A line trace in the 004 direction confirmed that the "symmetrized" image contained the expected a/4 (0.89Å) spacings (Fig. 5g).

Although symmetrization can be used for illustration, it has no ability to produce the correct relative phase (image peaks will not necessarily correspond to atom positions), and it cannot be used even for illustration unless specimen symmetry is known. To allow the OÅM to produce real sub-Ångstrom images, we corrected three-fold astigmatism with a hardware method proposed by Typke, using existing two-fold stigmator coils to produce an approximate three-fold field (Typke & Dierksen, 1995). The method reduced the OÅM three-fold astigmatism from 2.25µm to 0.03µm, negligible at the OÅM information limit (O’Keefe et al., 2001b).

After correction of the three-fold astigmatism, a “single-shot” image of [110] diamond obtained in the overlap range shows the expected symmetry (Fig. 5h); the C-C “dumbbells” can be clearly observed at a spacing of 0.89Å (Wang et al., 1999). The diffractogram (Fig. 4i) from the three-fold-corrected image has a much stronger 004 peak than the diffractogram of the uncorrected image, corresponding to better transfer of the 0.89Å information (since the contributing 004•000 and 000•00$\bar{4}$ diffracted beam interferences are no longer oppositely phased by three-fold astigmatism).

Focal-Series Reconstruction

As a final test of the OÅM’s ability to image diamond we used a focal series of twenty diamond images reconstructed to the exit-surface wave using the Philips/Brite-Euram software for focal-series reconstruction by Coene and Thust (Coene et al., 1996; Thust et al., 1996). The phase of the ESW showed the expected dumbbells (Fig. 4j) more clearly than the “single-shot” image (O’Keefe et al., 2001b).

Resolution Test at the Information Limit

Since the information limit of the CM300FEG/UT-OÅM was estimated to be close to 0.78Å (fig.3b), a test was carried out to try and resolve silicon atoms separated by 0.784Å in a specimen tilted into [112] orientation. The test was successful after the Haefly HT tank was replaced with an improved FEI high-voltage tank with a lower high-voltage ripple. With the new HT tank, beam energy spread (including HT instabilities) was measured as 0.93eV with the Gatan image filter (GIF) at a gun extraction voltage of 4kV; it improved to 0.85eV when the extraction voltage was dropped to 3.5kV. After correction for GIF contributions to the measurements, the true energy spreads were determined to be 0.85eV and 0.76eV respectively (O'Keefe et al., 2002) corresponding to an improvement in the CM300FEG/UT-OÅM information limit from 0.78Å at 4kV extraction voltage to 0.74Å at 3.5kV.

At 3.5kV extraction voltage, alpha-null defocus gave a noisy image (fig.6a) with pairs of white peaks that were often blurred together (O'Keefe et al, 2001a) but sometimes showed clear separation (fig.6b). A subsequent focal-series reconstruction of the phase of the exit wave (fig.6c) from 19 images produced a less noisy image with softer peaks barely separated (fig.6d). Since imaging (and reconstruction) conditions are close to the microscope's information limit, the peak separation is weak. However, from such a reconstruction of a defect area it would be possible to determine atom positions in the defect when atoms are separated by 0.78Å or more.

Both the 0.89Å diamond and 0.78Å silicon results demonstrate how atom positions can be obtained using the CM300FEG/UT with TrueImage at very high resolutions, then used to determine specimen structure (O'Keefe, 2004).

LITHIUM RESULTS

Following the successful imaging of carbon atoms separated by 0.89Å and silicon atoms separated by 0.78Å, we studied the imaging of lighter atoms in the presence of heavy ones by using the OÅM-CM300FEG/UT to investigate a specimen of $LiCoO_2$, the most commonly used positive electrode materials in lithium rechargeable batteries for portable electronic applications such as laptop computers. The mechanism of energy storage is based on lithium insertion and extraction from the CoO_2 host structure, so atomic arrangements of lithium ions have a profound effect on the electrochemical performance. One objective of the study was to attempt to atomically resolve lithium ions in the $LiCoO_2$ specimen.

The $LiCoO_2$ structure consists of CoO_2 octahedra with chains of Li atoms between. The unit cell is hexagonal with a = b = 2.816Å and c = 14.05Å. In [110] projection the two-dimensional cell is 2.44Å by 14.05Å with columns of Li atoms arranged in rows (Fig. 6).

As a first check on the resolution required to observe Li, we computed a series of images from a model of the structure using the weak-phase object approximation (Cowley & Iijima, 1972) over the resolution range 2Å to 0.4Å. The series showed that Co atoms would be visible at 2Å resolution, and that oxygen atoms would appear at 1.4Å resolution (Fig. 6). The lithium atoms would be visible at 1.0Å resolution, and would become clear at 0.8Å, where all three atom species are clearly distinguished.

Using the Cowley-Moodie multislice theory (Cowley & Moodie, 1957b), we next computed the phase of the exit-surface wave for resolutions from 0.8Å to 1.2Å with increasing specimen thickness from 1 to 40 unit cells thick. For the unit cell repeat of 2.816Å in the incident beam direction, the series covers 2.8Å to 113Å. The phase images did not change significantly in the resolution range from 0.8Å to 1.0Å. The first eighteen of the 0.9Å images are shown in figure 7, spanning a thickness range from 1 unit cell (3Å) to 18 unit cells (51Å) in steps of one unit cell. For small thickness (up to 6 unit cells), the heights of the white peaks corresponding to the atom positions are proportional to the scattering power of the atoms weighted by the specimen thickness (the number of atoms in the column under the beam). Oxygen atoms become visible by 4 to 6 unit cells (17Å), and lithium atoms by 10 to 12 unit cells (30Å).

At 8 unit cells (23Å) the phase of the electron wave at the Co position exceeds π and its peak becomes black, leaving the oxygen as the brightest peak. From 12 to 18 unit cells, the oxygen and lithium peaks increase, and the cobalt peak grows from -π to become white at 15 unit cells (42Å). In the thickness range from 14 to 18 unit cells, oxygen atoms appear as distinct white dots, cobalt atoms are increasingly bright but "fuzzy", and lithium atoms are weak (Fig. 7).

Plots of the ESW phase at the atom positions show the almost linear growth of the peaks with increasing specimen thickness, including the steep growth of the Co peak and the much slower growth of the oxygen and lithium peaks (Fig. 8). The oxygen peak flips phase at 22 unit cells (62Å), but the lithium peak remains below π up to a thickness of 40 unit cells (113Å). The Co peak becomes broader (the spot becomes fuzzy) with increasing thickness. The Li also becomes broader, while the oxygen peak appears not to broaden and the oxygen spot remains "sharp".

The OÅM was operated at 300keV and several focal series of images collected from $LiCoO_2$ samples in [110] orientation. The series were started at nominal defocus values of -3300Å and stepped back towards focus in increments of 24Å; each image required 1 second exposure and 5 seconds of CCD readout and defocus change, for a total acquisition time of 2 minutes. The phase image from an ESW reconstruction of 20 images shows all three types of atoms in the sample (Fig. 9a). Comparison with an ESW phase image simulated from the model at 17 unit cells thick (48Å) for 0.9Å resolution (Fig. 9b), shows that all the atom peaks have the characteristics predicted by the simulations. The O-Co-O units can clearly be distinguished, with each fuzzy Co atom flanked by a pair of bright oxygen atoms (Shao-Horn et al., 2002, 2003).

The weak peaks lying between them can be identified as coming from the lithium atoms (arrowed).

An additional check was carried out by running another set of ESW simulations on a model with the Li atoms removed. ESW phase images from this model show no sign of the Li peaks present in the images from the correct structure model. The weak white spots present in the experimental reconstruction appear in the simulation only when the model has the Li atoms present (Fig.10).

DISCUSSION

It is clear that improved resolution facilitates the imaging of light atoms in compound specimens. At first sight, it appears that 1.54Å resolution would be sufficient to separate atoms 1.54Å apart (the distance between the projected positions of the Li atom and the nearest oxygen). However, it turns out that criteria for the observation of light atoms in the presence of heavier atoms are not met merely by selecting a resolution equal to the distance between the light atom and its neighbors. The tails produced by the "point-spread" functions generated by the interaction of the electron beam with the surrounding atoms can obscure or even suppress the signal coming from the light atom. In $LiCoO_2$, it requires sampling at 1.0Å resolution before the Li atom emerges from the "wakes" generated by its neighbors (figure 6).

The appearance of oxygen atoms in $LiCoO_2$ at 1.4Å (figure 6) is consistent with previous observations at this resolution (Horiuchi et al., 1991; Wenk et al., 1992; Jia & Thust, 1999; Jia et al., 2003). Imaging of lighter atoms, such as lithium, requires even better resolution, especially if "atom shape" (peak shape) in the image is to be close to the symmetrical shape of the atom in the specimen. Note that the peaks representing the atoms remain non-circular, due to the influence of surrounding atoms, until extremely high resolutions. Although this effect is most often more noticeable for lighter atoms in the presence of heavy ones, even the Co atoms are distinctly non-circular until resolution is improved from 2Å to 1.4Å (figure 6). The oxygen atoms are visible at 1.4Å, but do not become round until 0.6Å. The lightest atoms, Li, are most influenced by the presence of other atoms; although they are visible at 1.0Å resolution, they remain non-circular until 0.4Å. Because the shape effect is caused by the presence of adjoining atoms, it will be strongly specimen dependent.

In our results for $LiCoO_2$, the match between experiment and simulation is not exact. Comparison of the experimental result with the on-axis simulation shows that the specimen was slightly tilted away from the exact zone axis, smearing the oxygen peaks along the diagonal from top right to bottom left and displacing the lithium peaks from their central positions between the O-Co-O units. There may also be some electron beam damage causing atom displacement or specimen buckling (top left and bottom left).

It is known that specimen tilt reduces dynamical electron scattering, thus making the specimen appear thinner than the simulation (O'Keefe & Radmilovic, 1993). For this reason, it is likely that the physical thickness of our tilted specimen is somewhat greater than the 48Å indicated by the matching simulation of the ESW phase.

CONCLUSIONS

The imaging of lithium completes the range of atoms detectable by HRTEM (except, of course, for H and He). This range now extends from the heavy metals, through non-metals like silicon, oxygen, nitrogen and carbon, to the lightest of all the metals. With the range complete, the HRTEM is confirmed in its position as the preferred instrument for the imaging of atoms. The emergent nanotechnology revolution requires "eyes" – it must be possible to "see" what we have built – and HRTEM at sub-Ångstrom resolution will play an essential role. Our results with the OÅM-CM300FEG/UT foreshadow those to be expected from next-generation TEMs with C_S-corrected lenses and monochromated electron beams.

ACKNOWLEDGEMENTS

This report was originally written as a tribute to Professor J.M. Cowley on the occasion of his 80th birthday. The first author is especially grateful to Professor Cowley for his guidance on the road that has led to the achievement of sub-Ångstrom resolution and the imaging of light atoms. John Cowley will be sorely missed. This work was supported by the Director, Office of Science, Office of Basic Energy Sciences, Material Sciences Division, of the U.S. Department of Energy, under contract No. DE-AC03-76SF00098 Additional support was provided by National Science Foundation International Research Fellow Award INT-0000429. Electron microscopy was performed at the J.M. Cowley Center for HREM at Arizona State University, and at the NCEM at Lawrence Berkeley National Laboratory. The authors would like to acknowledge Sumio Iijima, C.J.D. Hetherington, E. Chris Nelson, Andreas Thust and Christian Kuebel for their help.

REFERENCES

ALLPRESS, J.G. (1969). The direct observation of structural features and defects in complex oxides by two-dimensional lattice imaging. *Mat. Res. Bull.* **310**, 707-712.

ALLPRESS, J.G., HEWAT, E.A., MOODIE, A.F. & SANDERS, J.V. (1972). **n**-beam lattice images, I. Experimental and computed images from $W_4Nb_{26}O_{77}$. *Acta Cryst.* A**28**, 528-535.

ANSTIS, G.R., LYNCH, D.F., MOODIE, A.F. & O'KEEFE, M.A. (1973). **n**-beam lattice images, III. Upper limits of ionicity in $W_4Nb_{26}O_{77}$. *Acta Cryst.* A**29,** 138-147.

ANSTIS, G.R. & O'KEEFE, M.A. (1976). Resolution-limiting effects in electron microscope images. *34th Ann. Proc. EMSA*, Miami Beach, 480-481.

BAKKER, H., BLEEKER, A. & MUL, P. (1996). Design and performance of an ultra-high-resolution 300 kV microscope. *Ultramicroscopy* **64** (1996) 17-34.

COENE, W.M.J., THUST, A., OP DE BEECK, M., & VAN DYCK, D. (1996). Maximum-likelihood method for focus-variation image reconstruction in high resolution transmission electron microscopy. *Ultramicroscopy* **64**, 109-135.

COOK, J.M., O'KEEFE, M.A., SMITH, D.J. & STOBBS, W.M. (1983). The high resolution electron microscopy of stacking defects in Cu-Zn-Al shape-memory alloy. *J. Microscopy* **129**, 295-306.

COWLEY, J. M. & MOODIE, A. F. (1957a). Fourier images. I. The point source. *Proc. Phys. Soc.* B **70** (1957) 486-496.

COWLEY, J. M. & MOODIE, A. F. (1957b). The scattering of electrons by atoms and crystals. I. A new theoretical approach. *Acta Cryst.* **10**, 609-623.

COWLEY, J. M. & IIJIMA, S. (1972) Electron microscope image contrast for thin crystals. *Z. Naturforsch.* **27a**, 445-451.

DEN DEKKER, A.J. & VAN DEN BOS, A. (1997). Resolution: a survey. *Journal of the Optical Society of America A* **14**: (3) 547-557.

DOWNING, K.H., MEISHENG, HU, WENK, H.-R & O'KEEFE, M.A. (1990). Resolution of oxygen atoms in staurolite by three-dimensional transmission electron microscopy. *Nature* **348,** 525-528.

EPICIER, T., O'KEEFE, M.A. & THOMAS, G. (1990). Atomic imaging of 3:2 mullite. *Acta Cryst.* A**46**, 948-962.

FRANK, J. (1973). The envelope of electron microscopic transfer functions for partially coherent illumination. *Optik* **38**, 519-536.

HAIDER, M., BRAUNSHAUSEN, G. & SCHWAN, E. (1995). Correction of the spherical aberration of a 200kV TEM by means of a hexapole-corrector. *Optik*, **99**, 167-179.

HORIUCHI, S., MATSUI, Y., KITAMI, Y., YOKOYAMA, M., SUEHARA, S., WU, X. J., MATSUI, I. & KATSUTA, T. (1991). Ultra-high-resolution HVEM (H-1500) newly constructed at NIRIM. II. Application to materials. *Ultramicroscopy* **39**, 231-237.

IIJIMA, S. (1971). High resolution electron microscopy of crystal lattice of titanium-niobium oxide. *J. Appl. Phys.* **42**, 5891-5893.

IIJIMA, S. & O'KEEFE, M.A. (1979). Determination of defocus values using 'Fourier images' for high resolution electron microscopy. *J. Micros.* **117**, 347-354.

JIA, C. L. & THUST, A. (1999). Investigation of atomic displacements at a Σ3 {111} twin boundary in $BaTiO_3$ by means of phase-retrieval electron microscopy. *Phys. Rev. Letts* **82**, 5052-5055.

JIA, C. L., LENTZEN, M. & URBAN, K. (2003). Atomic-resolution imaging of oxygen in perovskite ceramics. *Science* **299**, 870-873.

KISIELOWSKI, C., HETHERINGTON, C. J. D., WANG, Y. C., KILAAS, R., O'KEEFE, M. A. & THUST, A. (2001). Imaging columns of the light elements carbon, nitrogen and oxygen at sub-Ångstrom resolution. *Ultramicroscopy* **89**, 243-263.

LICHTE, H. (1991). Optimum focus for taking electron holograms. *Ultramicroscopy* **38,** 13-22.

LYNCH, D.F. &. O'KEEFE, M.A. (1972). **n**-beam lattice images, II. Methods of calculation. *Acta Cryst.* A**28,** 536-548.

LYNCH, D. F., MOODIE, A. F. & O'KEEFE, M.A. (1975). **n**-beam lattice images, V. Use of the charge-density approximation in the interpretation of lattice images. *Acta Cryst.* A**31,** 300-307.

MALM, J.-O. & O'KEEFE, M.A. (1993). Using convergence and spread-of-focus parameters to model spatial and temporal coherence in HRTEM image simulations. *51st Ann Proc. MSA,* Cincinnatti, Ohio, 974-975.

O'KEEFE, M.A. (1973). **n**-beam lattice images, IV. Computed two-dimensional images. *Acta Cryst.* A**29**, 389-401.

O'KEEFE, M.A. & SANDERS, J.V. (1975). **n**-beam lattice images, VI. Degradation of image resolution by a combination of incident-beam divergence and spherical aberration. *Acta Cryst.* A**31**, 307-310.

O'KEEFE, M.A., BUSECK, P.R. & IIJIMA, S. (1978). Computed crystal structure images for high resolution electron microscopy. *Nature* **274,** 322-324.

O'KEEFE, M.A. (1979). Resolution-damping functions in non-linear images. *37th Ann. Proc. EMSA*, San Antonio, Texas 556-557.

O'KEEFE, M.A. (1992). Resolution in high-resolution electron microscopy. *Ultramicroscopy* **47**, 282-297.

O'KEEFE, M.A. (1993). Using coherent illumination to extend HRTEM resolution: why we need a FEG-TEM for HREM. *LBL Symposium on Microstructures of Materials,* edited by K. Krishnan (Berkeley: San Francisco Press), pp. 121-126.

O'KEEFE, M.A. (1998). Theoretical and practical aspects in computer simulation of high resolution transmission electron microscope images, *Proceedings of XIVth Int. Congress for Electron Microscopy* **1**, 2: 573-574.

O'KEEFE, M.A. (2001). Alpha-null defocus: an optimum defocus condition with relevance for focal-series reconstruction. *Microscopy & Microanalysis* **7**, 2: 916-917.

O'KEEFE, M.A. (2004). Image formation in the high-resolution transmission electron micro-scope, *Microscopy & Microanalysis* **10**, 397-399.

O'KEEFE, M.A. & RADMILOVIC, V. (1993). The effects of small crystal tilts on dynamical scattering: why simulated images are thinner than experimental ones. *51st Ann Proc. MSA*, Cincinnatti, Ohio, 980-981.

O'KEEFE, M.A., NELSON, E.C., WANG, Y.C. & THUST, A. (2001a). Sub-Ångstrom resolution of atomistic structures below 0.8Å. Philosophical Magazine B **81,** 11: 1861-1878.

O'KEEFE, M.A., HETHERINGTON, C.J.D., WANG, Y.C., NELSON, E.C., TURNER, J.H., KISIELOWSKI, C., MALM, J.-O., MUELLER, R., RINGNALDA, J., PAN, M., & THUST, A. (2001b). Sub-Ångstrom high-resolution transmission electron microscopy at 300keV. *Ultramicroscopy* **89**, 4: 215-241.

O'KEEFE, M.A. & SHAO-HORN, Y. (2004). Sub-Ångstrom atomic-resolution imaging from heavy atoms to light atoms. *Microscopy & Microanalysis* **10**, 86-95.

O'KEEFE, M.A., TIEMEIJER, P.C. & SIDOROV, M.V. (2002). Estimation of the electron beam energy spread for TEM information limit. *Microscopy & Microanalysis* **8**, 2: 480-481.

RAYLEIGH, LORD (a.k.a. STRUTT, J. W.). (1874). On the manufacture and theory of diffraction gratings. *Philosophical Magazine* **47**, 310: 81-93.

SCHERZER, O. (1949). The theoretical resolution limit of the electron microscope. *J. Applied Physics*, **20**, 20-29.

SCHISKE, P. (1973) in *Image Processing And Computer-Aided Design,* Ed. P.W. Hawkes, Acad. Press, London, pp.82-90.

SHAO-HORN, Y., O'KEEFE, M.A., NELSON, E.C., CROGUENNEC, L. & DELMAS, C. (2002). Atomic resolution of lithium ions in $LiCoO_2$. *Fall Meeting of the Materials Research Society*, *Symposium G*, Boston, Massachusetts.

SHAO-HORN, Y., CROGUENNEC, L. & DELMAS, C., NELSON, E.C., O'KEEFE, M.A. (2003). Atomic resolution of lithium ions in $LiCoO_2$. *Nature Materials* **2**, 464-467; advance on-line publication 15 June 2003 (doi: 10.1038/nmat922).

THUST, A., COENE, W.M.J., OP DE BEECK, M., & VAN DYCK, D. (1996). Focal-series reconstruction in HRTEM: simulation studies on non-periodic objects. *Ultramicroscopy*, **64**, 211-230.

TYPKE, D. & DIERKSEN, K. (1995). Determination of image aberrations in high-resolution electron microscopy using diffractogram and cross-correlation methods. *Optik* **99**, 4: 155-166.

VAN DYCK, D. & OP DE BEECK, M. (1990). New direct methods for phase and structure retrieval in HREM. *Proceedings of the 12th International Congress for Electron Microscopy*, edited by L.D. Peachy and D.B. Williams (Seattle, Washington), pp. 26-27.

WADE, R.H. & FRANK, J. (1977). Electron microscope transfer functions for partially coherent axial illumination and chromatic defocus spread. *Optik* **49**, 81-92.

WANG, Y.C., FITZGERALD, A., NELSON, E.C., SONG, C., O'KEEFE, M.A. & KISIELOWSKI, C. (1999). Effect of correction of the 3-fold astigmatism on HREM lattice imaging with information below 100 pm. *Microscopy & Microanalysis* **6**, 2: 822-823.

WENK, H.-R., DOWNING, K.H., MEISHENG, HU & O'KEEFE, M.A. (1992). 3d structure determination from electron-microscope images: electron crystallography of staurolite. *Acta Cryst*. A**48,** 700-716.

FIGURES

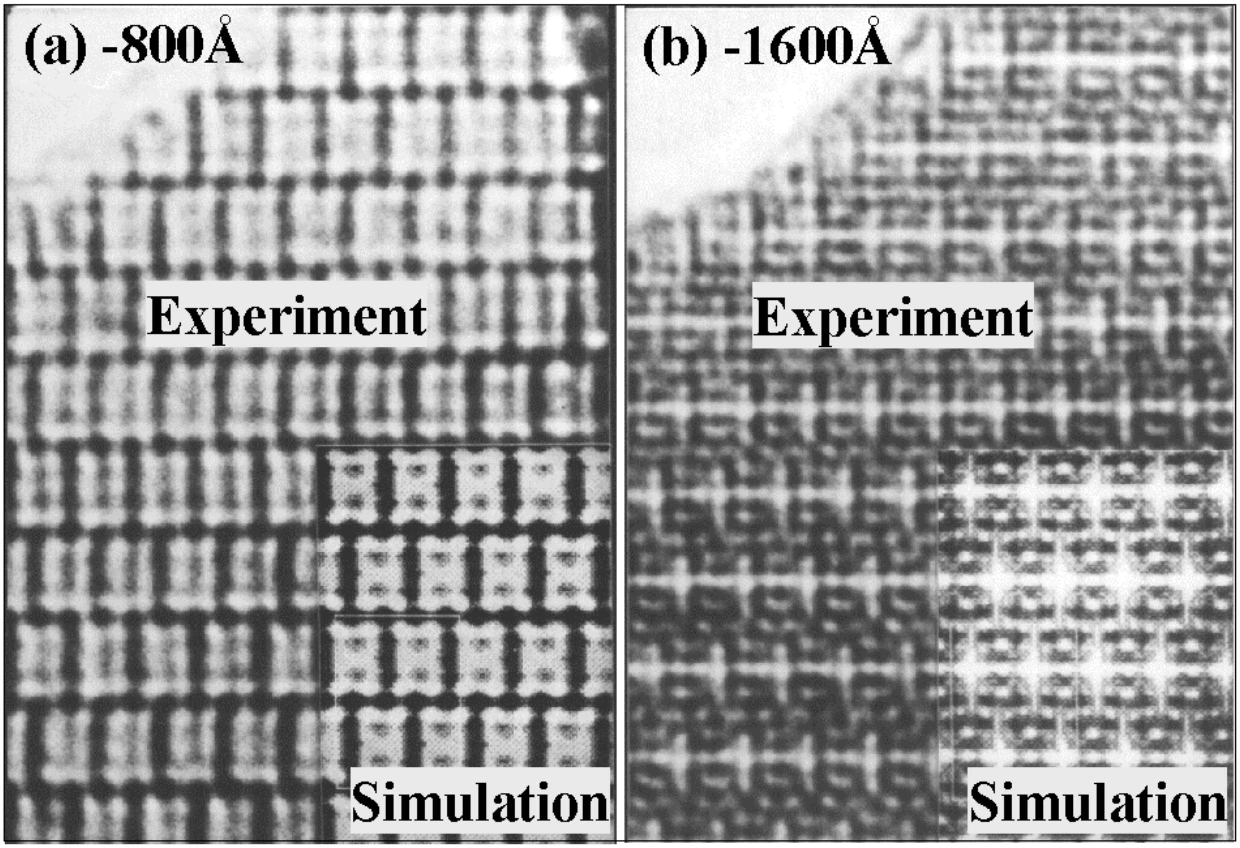

Figure 1. Pair of images of $Ti_2Nb_{10}O_{29}$ obtained on a JEOL 100B TEM shows smaller spacings at larger underfocus. **a**: Large 3x2 tunnels within the 4x3 blocks of metal-oxygen octahedra are visible as white dots at Scherzer defocus. **b**: At twice the underfocus, small tunnels between the 4x3 blocks of metal-oxygen octahedra are visible, but large tunnels are no longer seen.

[Reprinted from fig. 4 of *Nature* **274,** M.A. O'Keefe, P.R. Buseck and S. Iijima, "Computed crystal structure images for high resolution electron microscopy"**,** pp322-324, copyright (1978), with permission from Nature, http://www.nature.com].

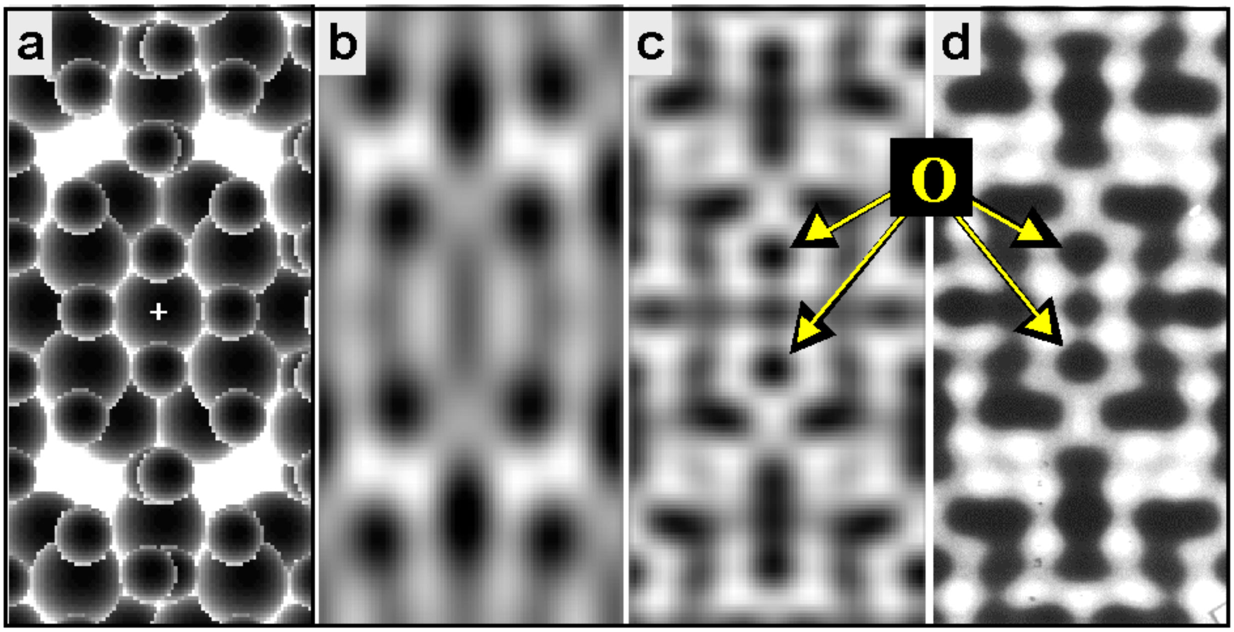

Figure 2. Focal series reconstruction improves resolution and images oxygen atoms. **a**: Model of staurolite in [001] projection; small spheres represent oxygen, large Al and Si. **b**: Averaged image from ARM-1000 (1.6Å resolution) at Scherzer defocus shows metal atoms. **c**: Image reconstructed from a focal series of five images shows oxygen atoms as well. **d**: Simulation at 1.4Å resolution. Arrows point to resolved oxygen atoms.

[Reprinted from figs. 9 & 10 of *Acta Cryst*. A**48,** H.-R. Wenk, K.H. Downing, Hu Meisheng and M.A. O'Keefe, "3d structure determination from electron-microscope images: electron crystallography of staurolite"**,** pp700-716, copyright (1992), with permission from IUCr, http://dx.doi.org/10.1107/S0108767392000850].

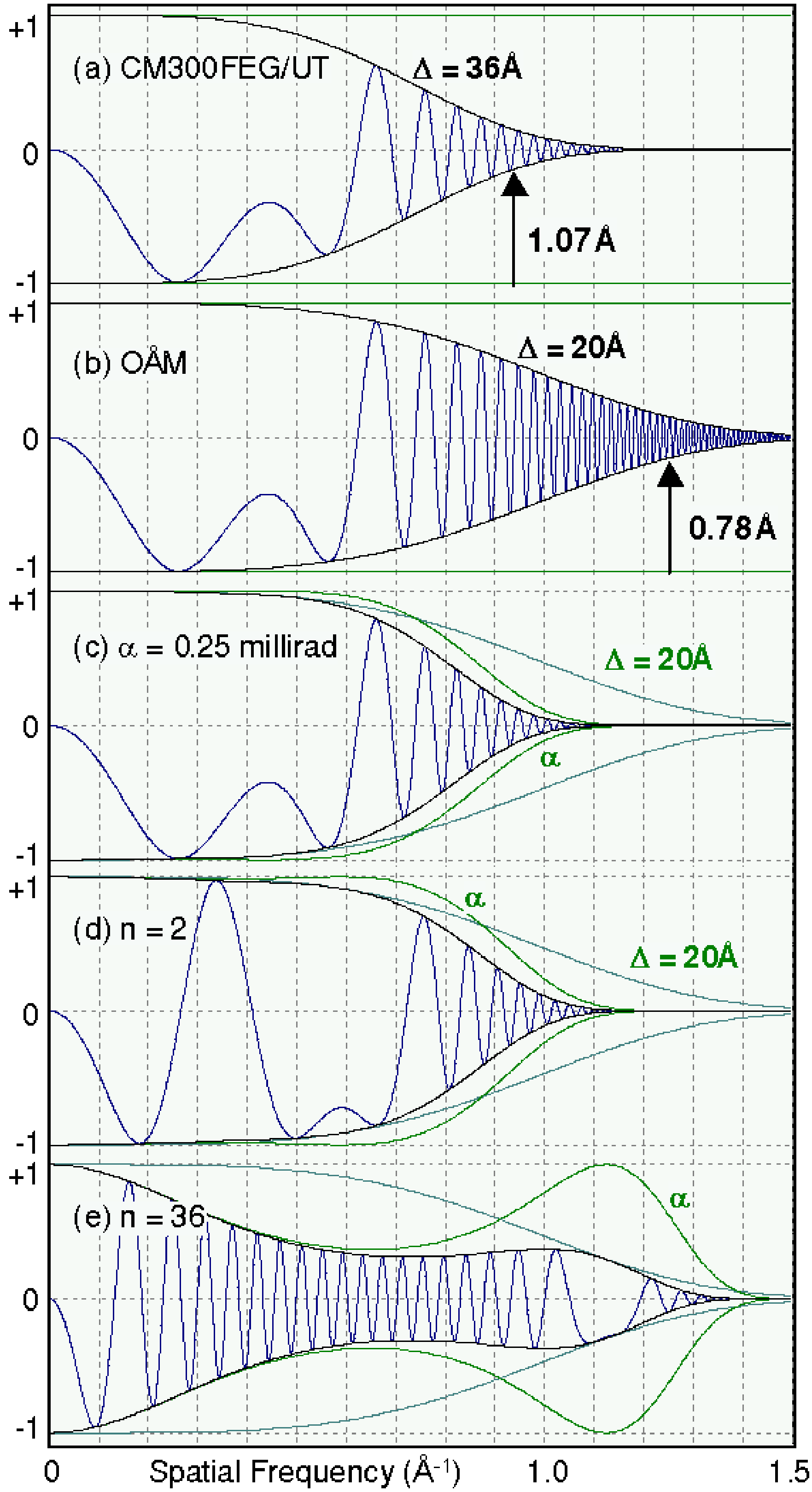

Figure 3. Contrast transfer functions out to 1.5Å^{-1} for 300keV electron energy and 0.6mm spherical aberration.

a: Standard CM300FEG/UT had 36Å spread of focus giving a 1.07Å information limit.

b: OÅM-CM300 has 20Å spread of focus and 0.78Å information limit.

c: Spatial coherence of 0.25 milliradian limits OÅM transfer at Scherzer defocus.

d: At second cross-over defocus (n=2), transfer moves to higher frequencies and mid-range frequencies become inverted.

e: For n=36 defocus, transfer extends to beyond 1Å.

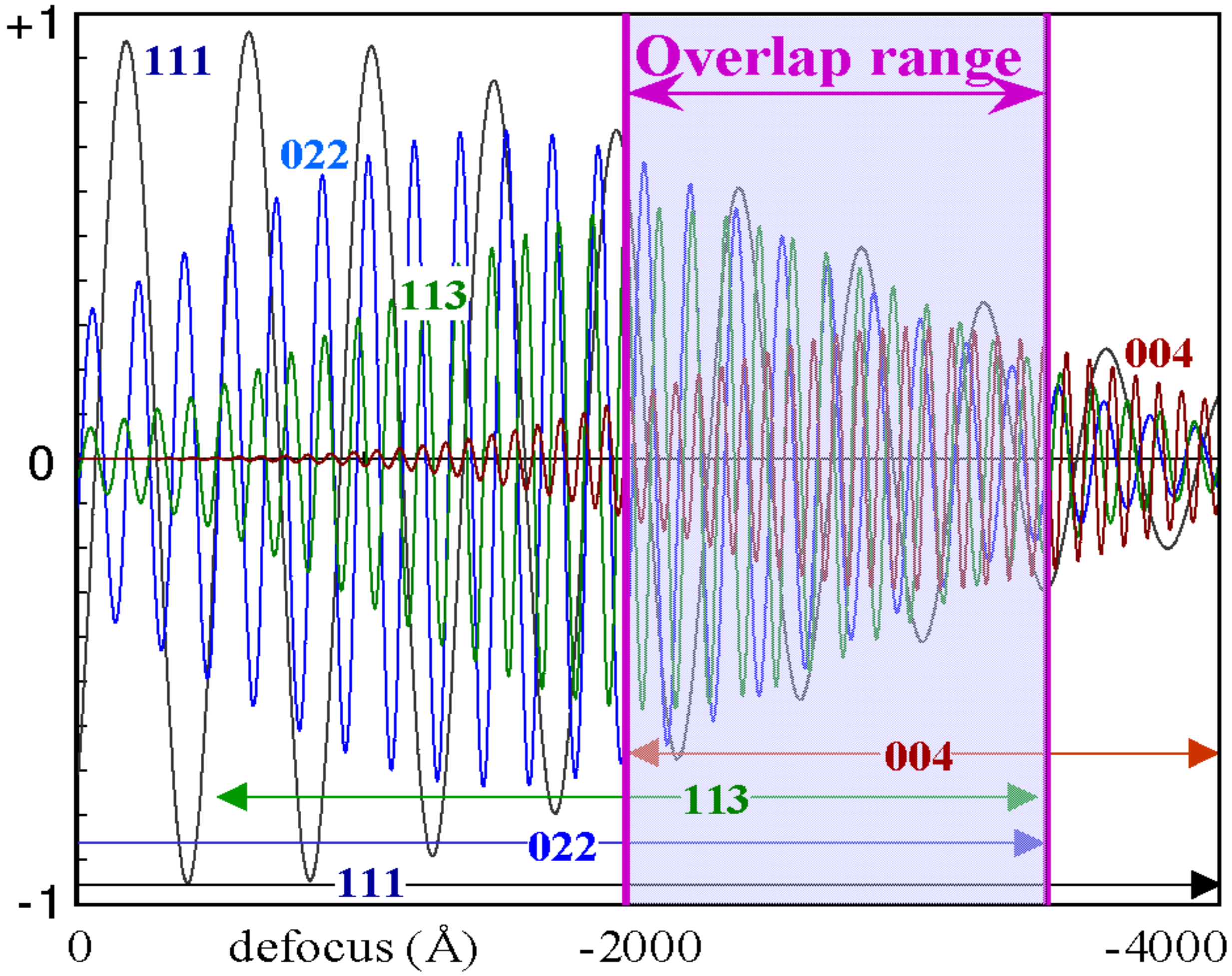

Figure 4. Focus-variation transfer functions at 300keV and C_S of 0.6mm for four sets of diffracted beams from [110] diamond. Packet limits (marked) create an overlap range in which all beams can contribute to a single image out to 0.89Å resolution.

[Reprinted from fig.12d of *Ultramicroscopy* **89**, M.A. O'Keefe, C.J.D. Hetherington, Y.C. Wang, E.C. Nelson, J.H. Turner, C. Kisielowski, J.-O. Malm, R. Mueller, J. Ringnalda, M. Pan and A. Thust, "Sub-Ångstrom High-Resolution Transmission Electron Microscopy at 300keV"**,** p234, copyright (2001), with permission from Elsevier, http://www.elsevier.nl/locate/ultramic. Reprinted from fig.6 of *Philosophical Magazine B* **81**, M.A. O'Keefe, E.C. Nelson, Y.C. Wang and A. Thust, "Sub-Ångstrom resolution of atomistic structures below 0.8Å"**,** pp1861-1878, copyright (2001), with permission from Taylor & Francis, http://www.tandf.co.uk].

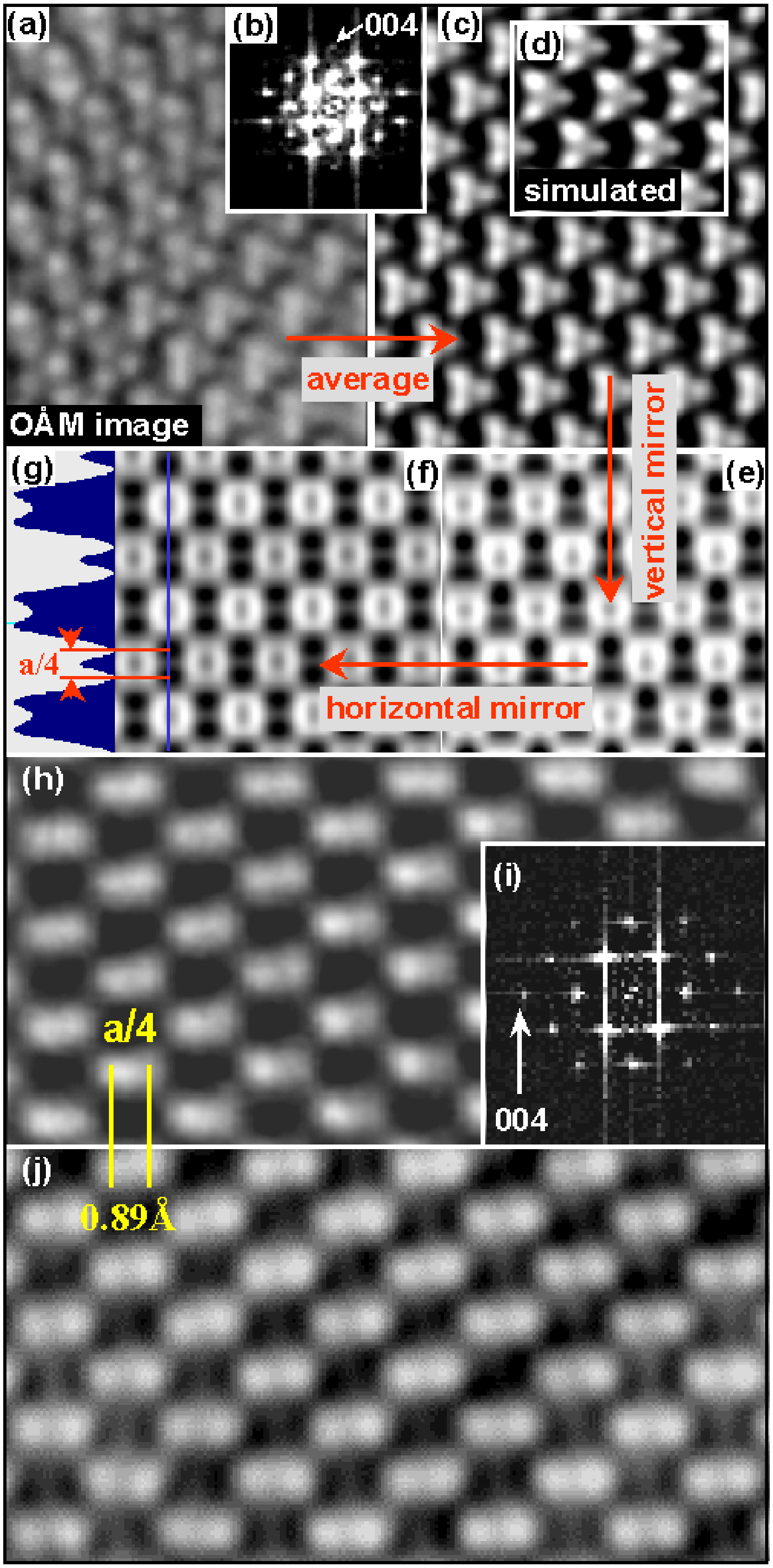

Figure 5. OÅM-CM300 diamond images in [110] orientation. **a**: Before correction of 3-fold astigmatism. **b**: Diffractogram has weak 004 spot. **c**: Averaged image. **d**: Simulation with 2.25 µm 3-fold astigmatism. **e**: Mirrored horizontally. **f**: Mirrored vertically. **g**: Line trace shows 0.89Å spacing. **h**: After correction of 3-fold astigmatism. **i**: Diffractogram has strong 004 spot. **j**: Phase of exit-surface-wave reconstruction from a focal series of 20 images.

[Parts of fig. 5 are reprinted from figs. 8, 10a & 15 of *Ultramicroscopy* **89**, with permission from Elsevier, http://www.elsevier.nl/locate/ultramic copyright 2001].

[Fig. 5h is reprinted from fig. 7 of *Philosophical Magazine B* **81**, M.A. O'Keefe, E.C. Nelson, Y.C. Wang and A. Thust, "Sub-Ångstrom resolution of atomistic structures below 0.8Å", pp1861-1878, copyright 2001, with permission from Taylor & Francis, http://www.tandf.co.uk].

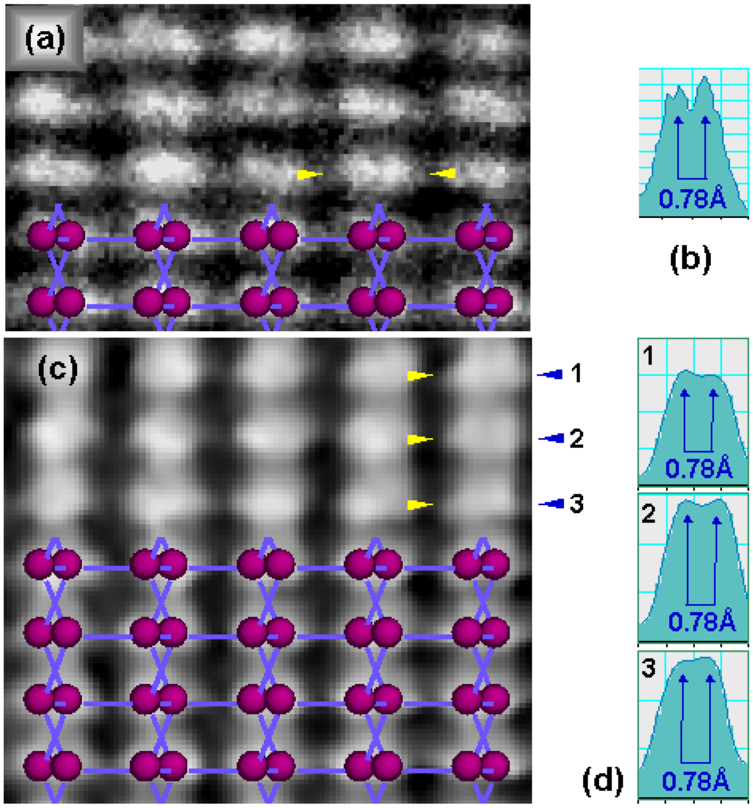

Figure 6. OÅM-CM300 images of silicon in [112] orientation.

a. Single-shot image taken near alpha-null defocus shows pairs of silicon atoms separated by 0.78Å.

b. Profile of double peak (marked in **a**) shows clear peak separation.

c. OÅM image reconstructed from a 19-member focal series.

d. Profiles of three atom pairs (marked in **c**). Both images have superimposed models of silicon in [112] orientation, and profiles have 0.784Å scale bars.

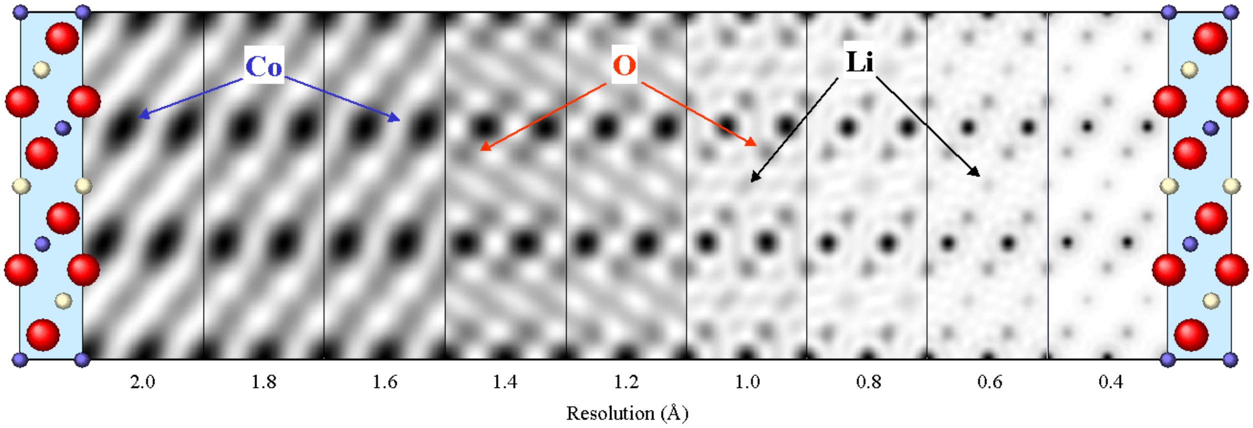

Figure 7. $LiCoO_2$ model (left and right) projected in [110] direction shows horizontal rows of Li, Co and O atoms within cell of size 2.44Å by 14.05Å. Weak-phase-object image series (black atoms) simulated in [110] orientation for increasing resolution (marked) shows atoms: Co at 2Å, O at 1.4Å, and Li at 1Å. Each image shows 2 by 1 unit cells.

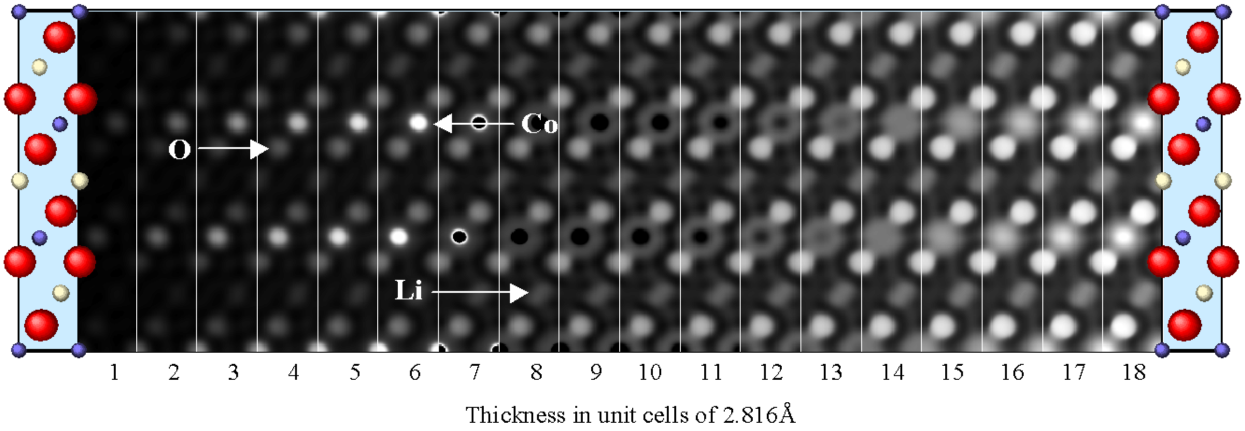

Figure 8. $LiCoO_2$ model and ESW-phase images in [110] orientation. Images simulated at 0.9Å resolution for increasing specimen thickness (marked in unit cells of 2.816Å). Arrows point to horizontal rows of Co, O, and Li atom columns. Each image shows 1 unit cell.

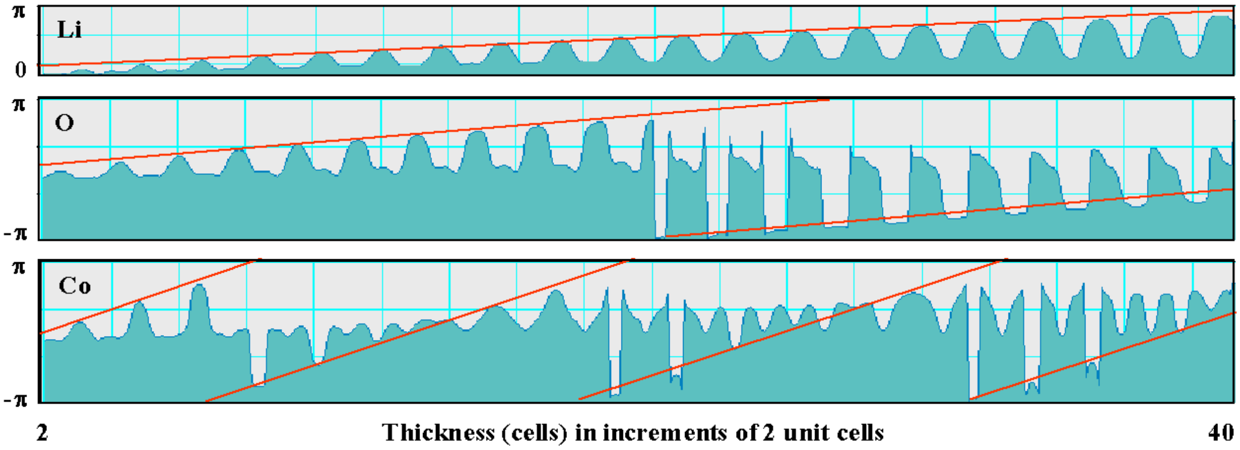

Figure 9. Profiles across phase of simulated $LiCoO_2$ ESW images show phase increases at atom positions for increasing specimen thickness. Slope of phase increase is higher for heavier atoms.

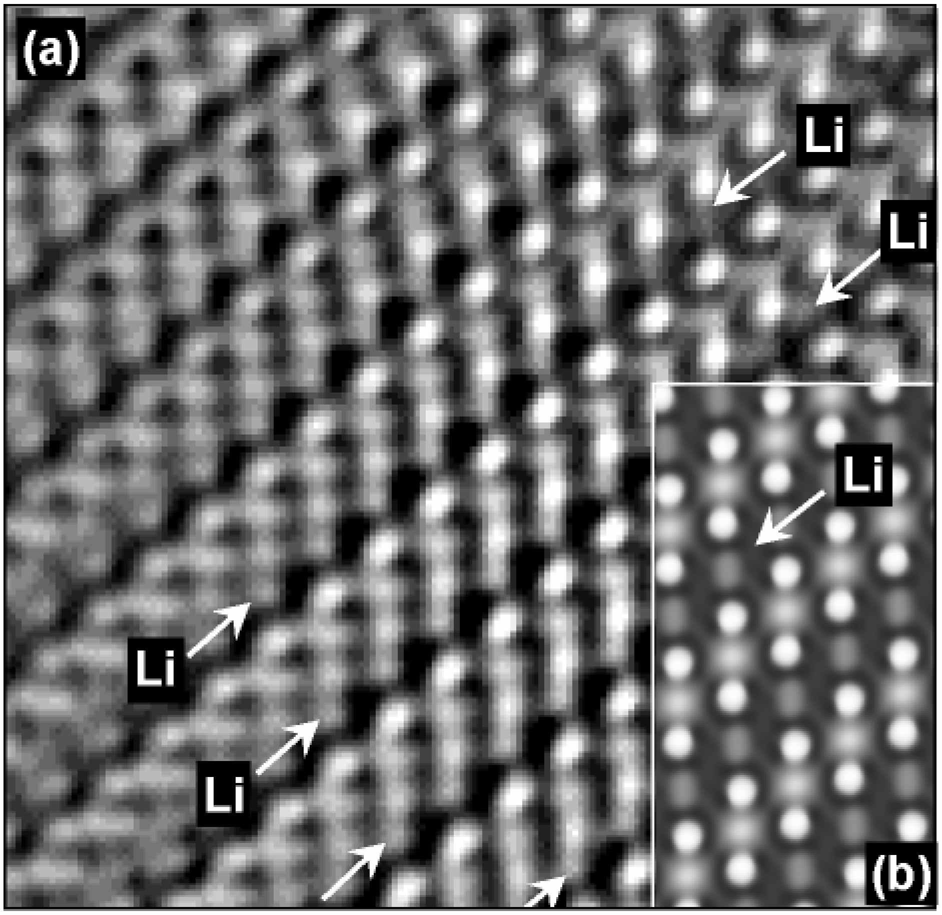

Figure 10. **a**: $LiCoO_2$ ESW-phase image, reconstructed from 20 experimental images, shows rows of Li atoms between O-Co-O groups. **b**: Inset ESW-phase simulation for 48Å thickness.

[Reprinted from fig. 4 of *Nature Materials* **2,** Yang Shao-Horn, Laurence Croguennec, Claude Delmas, E. Chris Nelson & Michael A. O'Keefe, "Atomic resolution of lithium ions in $LiCoO_2$"**,** pp464-467, advance on-line publication 15 June 2003 (doi: 10.1038/nmat922), copyright (2003), with permission from Nature, http://dx.doi.org/10.1038/nmat922].

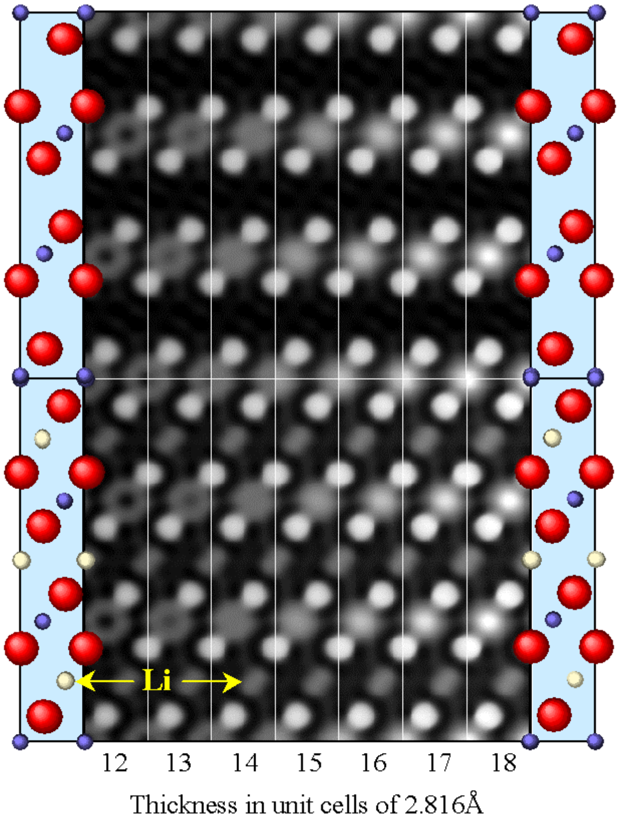

Figure 11. $LiCoO_2$ models and ESW-phase images in [110] orientation for $LiCoO_2$ without lithium atoms (upper) and with lithium atoms (lower). Images are simulated at 0.9Å resolution for increasing specimen thickness (marked in unit cells of 2.816Å). Arrows point to horizontal row of Li atom columns. Each image shows 1 unit cell.